First principles calculations of optical properties for oxygen vacancies in binary metal oxides

Jack Strand,[1, a)] Sergey K. Chulkov,[2, b)] Matthew B. Watkins,[2, c)] and Alexander L. Shluger[3, d)]
[1)] *Department of Physics and Astronomy, University College London, Gower Street, London, WC1E 6BT, United Kingdom*
[2)] *School of Mathematics and Physics, University of Lincoln, Brayford Pool, Lincoln LN6 7TS, United Kingdom*
[3)] *Department of Physics and Astronomy and London Centre for Nanotechnology, University College London, Gower Street, London, WC1E 6BT, United Kingdom*

Using an advanced computational methodology implemented in CP2K, a non-local PBE0-TC-LRC density functional and the recently implemented Linear Response formulation of the TD-DFT equations we test the interpretation of the optical absorption and photoluminescence signatures attributed by previous experimental and theoretical studies to O-vacancies in two widely used oxides – cubic MgO and monoclinic (m)-HfO_2. The results obtained in large periodic cells including up to 1000 atoms emphasize the importance of accurate predictions of defect-induced lattice distortions. They confirm that optical transitions of O-vacancies in 0, +1 and +2 charge states in MgO all have energies close to 5 eV. We test the models of photoluminescence of O-vacancies proposed in the literature. The photoluminescence of V_O^{+2} centers in m-HfO_2 is predicted to peak at 3.7 eV and originate from radiative tunneling transition between a V_O^{+1} center and a self-trapped hole created by the 5.2 eV excitation.

I. INTRODUCTION

Oxygen vacancies strongly affect physical and chemical properties of oxides and have been studied extensively both experimentally and theoretically[1–4]. Experimental identification of such defects in bulk materials often relies on the interpretation of recorded optical absorption, photo-luminescence, and electron paramagnetic resonance spectra. Surprisingly, spectroscopic signatures of O vacancies in different charge states are not well established even in case of the simplest oxides, such as MgO. This complicates verification of existence of O vacancies as well as models and hypothesis attributed to effects of their presence. In this paper we test the interpretation of optical absorption and photoluminescence signatures attributed in the literature to O vacancies in two widely used metal oxides – cubic MgO and monoclinic (m)-HfO_2.

MgO has long been studied as a model wide band gap oxide with numerous technological applications. Extensive experimental studies have been carried out of defects in MgO, and particularly O-vacancy (also known as an F center)[5–10]. Theoretical studies, however, still struggle to give reliable insights into the optical spectra of different charge states of this defect. For example, theoretical models still continue to disagree on the exact positions of optical absorption peaks of neutral and positively charged vacancies. The first optical absorption peaks of the neutral and +1 charged oxygen vacancies (V_O^0 and V_O^{+1} centers) occur at very similar energies: 5.01 and 4.96 eV, respectively[5]. These peaks are difficult to resolve both experimentally and in theoretical calculations. *Ab initio* cluster model calculations of V_O^0 and V_O^{+1} defects[11] predicted very similar optical absorption energies, however, the absolute value was closer to 6 eV, rather than the experimental 5 eV. It was argued that the main source of error in this study was the limited basis set size and that 3d polarization functions should be added to the oxygen basis set. Further calculations[12] using a larger basis set predicted the optical absorption energy for V_O^0 at 5.44 eV, in closer agreement with experiment. The optical excitation energy for the V_O^{+1} defect, however, was not improved. It was therefore concluded that much larger basis sets are necessary for accurate prediction of the optical absorption spectrum. In both of these studies only excitations in the alpha spin channel were reported for the V_O^{+1} center. However, there are, in fact, two types of optical excitation in the V_O^{+1} center (see Fig. 1): a type-V transition into a higher state located close to the bottom of the conduction band (CB) in the α-spin channel, and a type-III transition from the defect-induced valence band states into the unoccupied state associated with the V_O^{+1} center in the β-spin channel.

The β channel excitation was suggested in previous theoretical and experimental studies[13,14] as a possible origin of the 5 eV absorption peak. Interestingly, both the α and β channel excitations (type V and III, correspondingly) in the V_O^{+1} center are predicted to be close to 5 eV. Thus, all three optical absorption peaks associated with V_O^0 and V_O^{+1} centers have very close energies. A qualitative difference between α and β spin excitation for the V_O^{+1} center, however, is that β channel excitations should be associated with the release of holes into the valence band (VB). It has been shown that, when exciting MgO crystals with 5 eV light, a 2.3 eV absorp-

[a)] Electronic mail: jack.strand.14@ucl.ac.uk
[b)] Electronic mail: schulkov@lincoln.ac.uk
[c)] Electronic mail: mwatkins@lincoln.ac.uk
[d)] Electronic mail: a.shluger@ucl.ac.uk

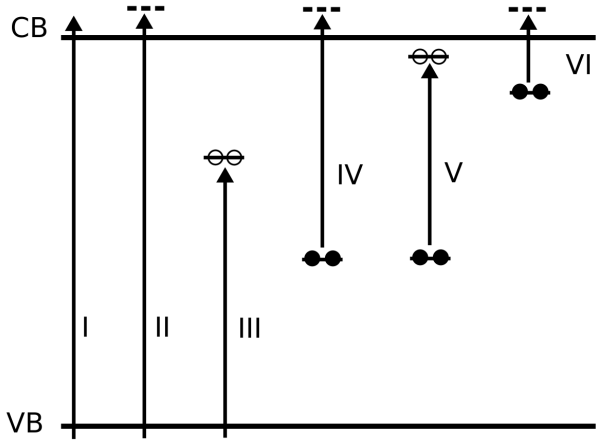

FIG. 1. Schematic of the typical optical transitions in oxides with defects. Type-I is a band-to-band transition. Type II is a VB to defect-induced unoccupied resonant state in CB transition. Type III represents the VB to unoccupied defect state in the bandgap transition. Type IV is an occupied defect state into defect-induced state in the CB transition, and type V is an occupied defect state into un-occupied defect state in the bandgap transition. A type VI transition is from a shallow, occupied defect state into the defect-induced resonant state in the CB.

tion band also develops, which is associated with holes trapped on V-type centers[13,14]. Recent periodic Density Functional Theory (DFT) calculations[15] account for different spin channel excitations in MgO using many-body perturbation theory in the G_0W_0 approximation and the Bethe-Salpeter approach. These calculations predicted the existence of a 3.6 eV absorption band in the V_O^{+1} center (in addition to the known 5 eV band in the α channel), which could be used to distinguish between the V_O^0 and V_O^{+1} centers. Thus the position and nature of optical absorption peaks of V_O^0 and V_O^{+1} centers in MgO remain controversial. They are revisited and discussed in more detail below in section III B.

MgO also has a photoluminescence (PL) band at 2.3 eV attributed to the V_O^0 center[8–10,16]. The nature of this luminescence has been discussed based on theoretical and experimental data in Refs.[16,17] but has not been confirmed by many-electron calculations. These models are tested and discussed in detail in section III C.

HfO_2 is another topical oxide with many properties attributed to O vacancies. This high dielectric permittivity oxide is being used both as a gate dielectric in modern transistors and as a reducible oxide in memory cells[18,19]. The existing and newly generated oxygen vacancies in HfO_2 have been implicated in degradation of these devices and play the central role in the electroforming process in Resistive Random Access Memory (RRAM) devices[20–23]. Again, spectroscopic signatures of these defects are still controversial.

Experimentally, there is a well characterized 2.7 eV photoluminescence peak[24,25] associated with a 5.2 eV absorption peak. The optical transitions for all five charge states of the oxygen vacancy in m-HfO_2 were calculated in a DFT study using both periodic and embedded cluster methods and Time-dependent DFT (TD-DFT) for calculating optical transition energies[26]. These calculations predicted the absorption energy of the +2 charged oxygen vacancy (V_O^{+2} defect) at 4.94 eV, which is appreciably close to the 5.2 eV absorption peak. This provided evidence that the V_O^{+2} defect may be responsible for the 5.2/2.7 eV absorption/PL spectrum. Other experimental work on hafnia films has also connected this luminescence peak to oxygen vacancies. In a photoluminescence study[25]the 5.2 eV absorption and the 2.7 eV luminescence bands were interpreted as emerging from neutral (rather than positively charged) oxygen vacancies. Furthermore, another absorption/emission line - a 3.66 eV PL excited at 4.4 eV and 5.4 eV - has also been detected[27]. The predicted optical absorption energy for the neutral vacancy is approximately 3.2 eV[26]. This corresponds to an electron being excited out of a doubly occupied vacancy state (which has its Kohn-Sham (KS) level in the middle of the bandgap) into an unoccupied state at the bottom of CB (type V excitation in Fig. 1) . These calculations also predict similar positions for absorption peaks of V_O^{-1}, V_O^0 and V_O^{+1} defects, which all have occupied states at similar energies in the bandgap.

Thus, rather surprisingly considering the amount of research which went into studies of these two materials, their optical absorption and photoluminescence (PL) spectra are far from being understood. Predictions of positions of defect optical absorption and PL peaks rely on several factors: accuracy of calculations of defect-induced lattice relaxation, which often requires large periodic cells or clusters; positions of defect levels should be accurately reproduced, which requires using non-local density functionals; techniques used to calculate optical excitation energies. Satisfying all these requirements is challenging and compromises are often made in favor of one of the variables. For example, small periodic cells are used to afford more computationally demanding calculations using the GW approximation and the Bethe-Salpeter approach for calculating optical spectra. More efficient but less accurate LDA calculations are used to optimize the defect geometry.

Here we attempt to satisfy all the requirements by using an advanced computational methodology implemented in CP2K, a non-local PBE0-TC-LRC density functional and the recently implemented Linear Response formulation of the TD-DFT equations. These are described in detail in section II and in Appendix. Using this method, within the adiabatic approximation we calculate the optical transition energies for the 0, +1, and +2 charged O vacancies in MgO and m-HfO_2 and estimate the photoluminescence energies for the V_O^0 and V_O^{+2} centers in MgO and m-HfO_2. The results emphasize the importance of accurate predictions of defect-induced lattice distortions. They confirm that optical transitions of O-vacancies in 0, +1 and +2 charge states in MgO all

have energies close to 5 eV. We qualitatively confirm the model proposed to explain the nature of 2.3 eV PL in MgO in Refs.[16,17]. The PL at 3.7 eV of V_O^{+2} centers in m-HfO_2 is predicted to originate from radiative tunneling transition between a V_O^{+1} center and a self-trapped hole.

II. METHODOLOGY

A. Computational details

All simulations were carried out using periodic boundary conditions and the implementation of DFT in the CP2K software package[28]. These calculations sample the Brillouin Zone only at the Γ point. To check the dependence of the results on the cell size, for MgO supercells of 216, 512 and 1000 atoms and for m-HfO_2 96 and 324 atom supercells were used. Since we consider the 96 atom cell to be too small, we only analyze HfO_2 defects and optical transitions for the 324 atom cell.

Charged defects in the periodic model are calculated using the neutralizing jellium background, as implemented in CP2K. In this paper we are mainly concerned with optical excitations of defects in particular charge states rather than their formation energies and transition levels, where charge corrections as well as potential alignment are important. TDDFT calculations include KS orbital energy differences, which are affected by the cell size as well as the extent of lattice distortion induced by charged defects. These effects are checked using periodic cells of increasing sizes.

The PBE0-TC-LRC exchange-correlation (XC) functional[29] was used with an exact exchange contribution of 32.5% for the MgO calculations and 25% for the HfO_2 calculations. This functional is based on ordinary PBE0[30], however HF exchange is only used for ranges up to a selected "truncation radius". Beyond the truncation radius, a long range correction (based on the spherically averaged PBE exchange hole[31]) is applied. In this work, we use 6 Å for the truncation radius in MgO and 4 Å in HfO_2.

The GTH pseudopotentials and GTH MOLOPT basis sets were used for all atom species[32,33]. In our set up, Mg has 2 valence electrons, whereas Hf and O both have 6. All periodic cells had lattice parameters and geometry optimized such that forces were smaller than 0.023 eV/Å. The effect of oxygen vacancies on the local structure was simulated by re-optimizing the cell geometry after the deletion of an oxygen atom. Lattice parameters were kept constant during optimization of the defective cells. Since MgO has an FCC structure, all oxygen atoms in the periodic cell are equivalent and it is not necessary to sample different sites. In m-HfO_2 O atoms can be either 3- or 4-coordinated by Hf ions. In this work, we focus only on O vacancies at 3C sites. Positive or negative oxygen vacancies were simulated by removal or addition of electrons from the defective cell and then re-optimizing the geometry.

To calculate optical transition energies and oscillator strengths we use the well established Linear Response formulation of the TDDFT within the local adiabatic approximation. In this approximation, the XC-functional is simply one of the usual XC-functionals used for ground state DFT calculations. The detailed description of mathematical expressions implemented in CP2K is given in Appendix.

Calculation of Hartree-Fock electron-repulsion integrals greatly increases the computational cost of hybrid functionals, and renders the ground state DFT and TDDFT calculations infeasible for the system sizes considered here. For this reason it is necessary to employ the auxiliary density matrix method (ADMM)[34]. This approximation utilizes a smaller or faster converging basis set, greatly speeding up the calculation of HF exact exchange. This allows us to use large supercells, which means we can more fully represent the structural relaxation induced by the presence of vacancies. Reducing the basis set quality can introduce errors in the HF exchange calculations. The key assumption of ADMM are outlined in the next section.

B. Auxiliary Density Matrix Method

In ground-state KS-DFT the exact exchange energy, which is an essential component of hybrid XC-functionals, is expressed in terms of a density matrix P[34]:

$$E_x^{\mathrm{HF}}[P] = \sum_{\mu\nu\lambda\sigma} P_{\mu\lambda} P_{\nu\sigma} (\mu\nu|\lambda\sigma) \tag{1}$$

and Electron Repulsion Integrals (ERIs) over Gaussian basis functions $\{\chi\}$:

$$(\mu\nu|\lambda\xi) = \int \chi_\mu^*(\mathbf{r}) \chi_\nu(\mathbf{r}) \frac{1}{|\mathbf{r}-\mathbf{r}'|} \chi_\lambda^*(\mathbf{r}') \chi_\xi(\mathbf{r}') \mathrm{d}\mathbf{r}\mathrm{d}\mathbf{r}' \tag{2}$$

The number of such integrals grows with the total number of atomic basis functions to the fourth power in a naive implementation that quickly becomes a bottleneck. However, the majority of these integrals are negligible. In particular, the inner product of two Gaussian functions centred on different atoms exponentially decays with the distance between these atoms. This effectively means that the number of non-negligible ERIs scales quadratically with the system size for a given basis set.

To take advantage of this fact, CP2K screens ERIs based on the Cauchy-Schwarz inequality:

$$(\mu\nu|\lambda\sigma) \leq \sqrt{(\mu\nu|\mu\nu)} \sqrt{(\lambda\xi|\lambda\xi)}, \tag{3}$$

and ignores the integrals which are less than the given threshold. Screening based additionally on the size of the density matrix element of the pair of orbitals in the ground state wave function can further reduce this to linear scaling. However even in this case evaluation of ERIs

still remains a challenging task due to a large prefactor. This prefactor becomes much larger when the basis set is augmented with diffuse functions, because these functions have a slower long-range decay. This problem also affects the MOLOPT basis sets commonly used in CP2K[33], as they contain significant numbers of (contracted) diffuse basis functions.

The Auxiliary Density Matrix Method (ADMM) addresses this problem by computing ERIs using a small auxiliary basis set with rapidly decaying basis functions $\{\tilde{\chi}\}$. An approximate auxiliary density matrix $\tilde{P}$ is then constructed by fitting the density matrix in the primary basis set (P):

$$\tilde{P} = OPO^{\mathrm{T}}, \tag{4}$$

using a projector from the primary basis set onto the auxiliary basis set:

$$O = \tilde{S}^{-1}U, \tag{5}$$

$$\tilde{S}_{\mu\nu} = \langle\tilde{\chi}_\mu|\tilde{\chi}_\nu\rangle, \quad U_{\mu\nu} = \langle\tilde{\chi}_\mu|\chi_\nu\rangle. \tag{6}$$

Optionally, the ground-state auxiliary density matrix can be purified using a number of techniques[34] to ensure that all properties of a true density matrix are met. We have not implemented purification for use with TDDFT methods, as a response density matrix $P^{(1)}$ – which appears in Eq. (1) instead of the ground-state density matrix – does not satisfy all conditions for a pure density matrix (see Appendix for further details).

ADMM also assumes that the difference between exact-exchange energies computed using primary and auxiliary basis sets has (semi-)local nature and thus can be well described using some reference LDA or GGA exchange functional ($E_{\mathrm{x}}^{\mathrm{DFT}}$). It naturally leads to the trivial expression for the approximate exact-exchange energy in the primary basis set:

$$E_{\mathrm{x}}^{\mathrm{HF}}[P] \approx E_{\mathrm{x}}^{\mathrm{HF}}[\tilde{P}] + (E_{\mathrm{x}}^{\mathrm{DFT}}[P] - E_{\mathrm{x}}^{\mathrm{DFT}}[\tilde{P}]). \tag{7}$$

Differentiation of the above expression with respect to the density matrix gives the following contribution to the Kohn-Sham matrix[35]:

$$K_{\mathrm{x}}^{\mathrm{HF}} \approx F_{\mathrm{x}}^{\mathrm{DFT}} + O^{\mathrm{T}}(\tilde{K}_{\mathrm{x}}^{\mathrm{HF}} - \tilde{F}_{\mathrm{x}}^{\mathrm{DFT}})O, \tag{8}$$

where

$$(F_{\mathrm{x}}^{\mathrm{DFT}})_{\alpha\beta} = \int \chi_\alpha^*(\mathbf{r})v_x[P](\mathbf{r})\chi_\beta(\mathbf{r})\mathrm{d}\mathbf{r}, \tag{9}$$

$$(\tilde{F}_{\mathrm{x}}^{\mathrm{DFT}})_{\mu\lambda} = \int \tilde{\chi}_\mu^*(\mathbf{r})v_x[\tilde{P}](\mathbf{r})\tilde{\chi}_\lambda(\mathbf{r})\mathrm{d}\mathbf{r}, \tag{10}$$

$$(\tilde{K}_{\mathrm{x}}^{\mathrm{HF}})_{\mu\lambda} = \sum_{\nu\sigma}\tilde{P}_{\nu\sigma}(\tilde{\mu}\tilde{\nu}|\tilde{\lambda}\tilde{\sigma}), \tag{11}$$

and v_{x} is the (semi-)local reference exchange potential as a functional of the electron density.

III. RESULTS AND DISCUSSION

A. Properties of perfect crystals

We start from considering the calculated bulk properties for different cell sizes of MgO and m-HfO_2. All calculations are performed sampling the Brillouin zone at the Γ point. The band gap energies are calculated as the difference of Kohn-Sham (KS) energies and using TDDFT. The results shown in Tables I and II for MgO and m-HfO_2, respectively, demonstrate good agreement of lattice parameters with experimental reports. However the band gap of HfO_2 is slightly overestimated. We note that in both systems the TDDFT calculated optical band gap is lower than the KS band gap. This is because, unlike in GGA-based TDDFT, in hybrid TDDFT there is electron-hole interaction[36]. Excitation between delocalized band states creates an electron-hole pair which is confined within the simulation cell and thus has an artificially high electron-hole interaction energy. This explains why the difference between the KS and TDDFT band gap is greatest for small simulation cells where the electron-hole pair is more confined and thus the electron-hole interaction is greater.

	Cell Size			
	216	512	1000	Exp.
$\|\mathbf{a}\|$	4.21	4.21	4.21	4.211[37]
KS BG	7.7	7.7	7.8	-
Optical BG	7.1	7.4	7.5	7.78[6]

TABLE I. The lattice parameters (Å) and band gap values (eV) for bulk MgO. The optical band gap (BG) is calculated using TDDFT. Cell sizes are given in number of atoms.

	Cell Size		
	96	324	Exp.
$\|\mathbf{a}\|$	5.08	5.07	5.117[38]
$\|\mathbf{b}\|$	5.13	5.13	5.18[38]
$\|\mathbf{c}\|$	5.25	5.24	5.29[38]
β (degrees)	99.12	99.11	99.22[38]
KS BG	6.51	6.66	-
Optical BG	6.0	6.1	5.68[39]

TABLE II. The lattice parameters (Å) and band gap energies (eV) calculated for bulk m-HfO_2. The optical band gap (BG) is calculated using TDDFT.

B. Optical transitions of O vacancies

The removal of a neutral oxygen atom in the MgO or m-HfO_2 periodic cell leaves behind a neutral oxygen vacancy, V_O^0. Two electrons localize on the vacancy (see Fig. 2). These localized electrons occupy two degenerate

	Ionic Displacements	
MgO	Δ_{Mg}	Δ_O
V_O^0	0.02	0.01
V_O^{+1}	0.11	0.03
V_O^{+2}	0.20	0.08
HfO_2	Δ_{Hf}	Δ_O
V_O^0	0.01 to 0.08	0.02 to 0.09
V_O^{+1}	0.09 to 0.11	0.04 to 0.18
V_O^{+2}	0.19 to 0.24	0.07 to 0.39

TABLE III. The displacements (in Å) of the ions surrounding an oxygen vacancy in MgO and HfO_2. Δ_{Mg}, Δ_{Hf} and Δ_O In MgO, high symmetry means that all NN Mg ions are displaced equal amounts, as are all NNN oxygen ions. In HfO_2, however, the surrounding Hf and O ions are not displaced equally. For HfO_2, the range of displacements are shown.

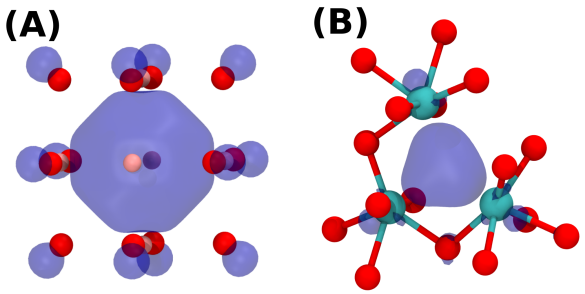

FIG. 2. The nearest-neighbor environment of neutral O-vacancy in MgO (A) and HfO_2 (B). An isosurface of the wavefunction of the doubly occupied defect state is shown in blue. Mg ions are colored in peach, Hf in cyan and O in red.

mid-gap levels (one state for each spin) which are located 4.45 eV below the conduction band minimum (CBM) in MgO and 3.3 eV below the CBM in HfO_2. In general, the vacancy perturbs the electronic structure, causing quasi-local states to appear in VB and CB, as shown in Fig. 1.

Structural relaxation around the neutral vacancy is small since the Coulomb interaction between the vacancy and nearby ions is similar to the Coulomb interaction between an oxygen ion and its neighbors in the bulk. Charging the vacancy causes greater structural reorganization. For example, charging the V_O^0 defect to the +1 state in MgO results in the nearest-neighbor Mg ions moving outward by 0.11 Å (See Table III). The calculated displacements are in good agreement with those derived from the analysis of EPR spectra of the V_O^{+1} center in Ref.[40].

In this study we look at the 0, +1 and +2 charge states of O vacancies in MgO and HfO_2. In the +1 charge state, the vacancy is paramagnetic. Removing an electron from V_O^0 (and then relaxing) to create a V_O^{+1} defect splits the doubly occupied state in the band gap into two states which are energetically separated. In MgO, for example, the occupied α spin state sits 5.2 eV below the CBM, whereas the β spin state is unoccupied and is higher in the band gap (see Fig. 1). The nature of the transition in the +1 state therefore depends on the spin channel: alpha spin excitations will involve a transition from a mid gap state into CB states, whereas a beta spin transition involves a VB electron being promoted into a gap state.

The wavefunctions of excited states calculated using TDDFPT are linear combinations of determinants where Ψ_i^a is a singly excited wave-function, whose i-th occupied Molecular Orbital (MO) is replaced by the a-th virtual MO (see Appendix). Often one excitation Ψ_i^a dominates and will be used to qualitatively represent the excited state in further discussion.

The lowest energy transition of the MgO V_O^0 defect has zero oscillator strength because the singly occupied defect state and the LUMO state dominating this transition have similar cubic symmetry (see Fig. 2) analogous to hydrogenic 1s and 2s orbitals. The next three higher energy transitions have equal excitation energies and are responsible for the main excitation peak seen in V_O^0 defects in MgO (Fig. 3(A)). They correspond to the excitation into a degenerate p-like state.

V_O^0 center in m-HfO_2 has lower symmetry and the TDDFT calculations predict a broader absorption spectrum with an onset at 2.5 eV, and then with higher energy peaks at 3.0 eV and 3.5 eV. Also, unlike in MgO, the V_O^0 excitation in HfO_2 is from the vacancy state into the states delocalized at the bottom of the conduction band. Hence much lower oscillator strengths of these transitions. The calculated spectra of the V_O^0 in HfO_2 are plotted in Fig. 3 (D). We note that the predicted transition energies are in good agreement with the results of embedded cluster calculations in Ref.[26].

In the +1 charge state, transitions in the α and β spin channels are no longer equivalent. In MgO, the absorption energies in both spin channels have been predicted to be close to one another[13], making the interpretation of optical absorption spectra difficult. Here, however, we predict that the β spin excitation has higher energy (Fig. 3(B)). This should lead to asymmetry in high energy part of the optical absorption spectrum of the V_O^{+1} center and can explain the asymmetric line shape observed in Ref.[7]. There will also be qualitative differences between the two types of excitation. Excitations in the α channel will excite an electron from the gap state into CB states, similar to the V_O^0 defect. Excitations in the β channel, however, will release holes into the valence band. It is then possible for these holes to be trapped onto V-centers[13].

We note that our results do not support the prediction[15] that the β absorption energy should be much lower than the α spin absorption energy ($\approx$ 3.6 eV). It is possible that the 3.6 eV absorption band emerges due to constraint on the V_O^{+1} center relaxation imposed by small periodic cells used in Ref.[15]. Indeed, charging the V_O^0 center to the +1 state but not allowing the structure to relax brings the main β-spin absorption energy down to 3.5 eV. This is not surprising as the defect-induced lattice distortion strongly affects the positions of quasi-local

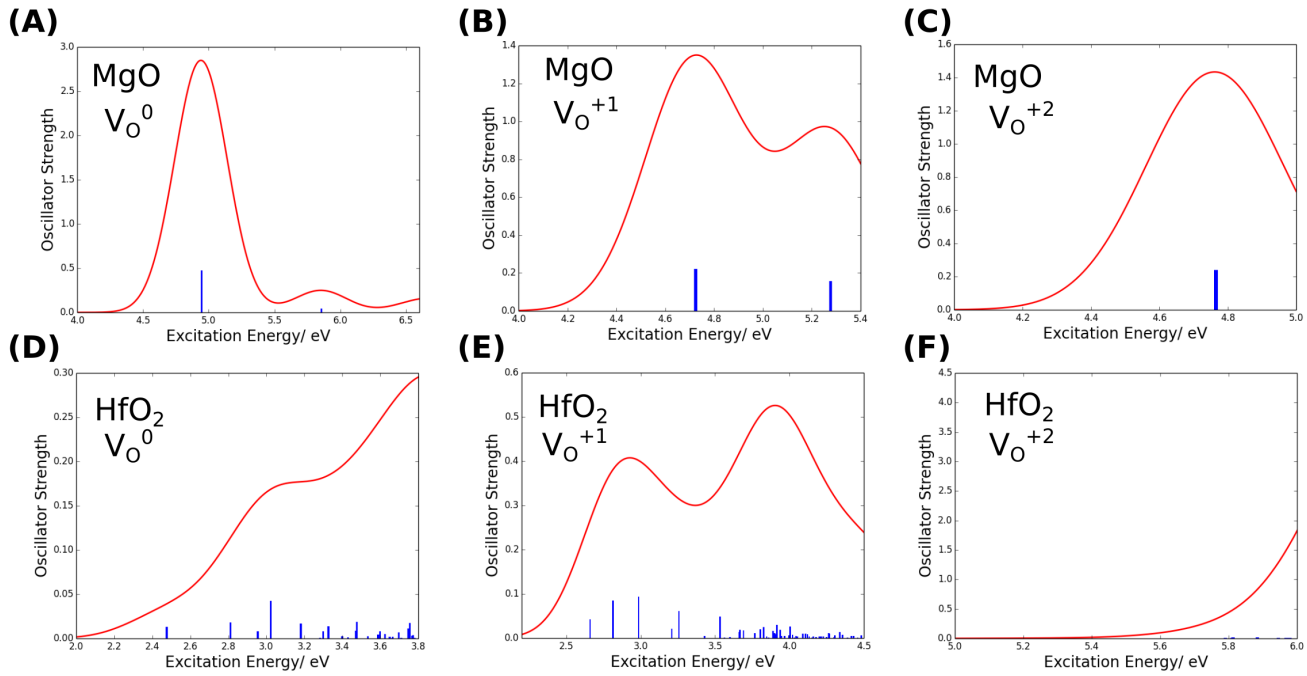

FIG. 3. Optical absorption spectra of oxygen vacancies in MgO and m-HfO_2. (A) is the V_O^0 defect in MgO. There is strong absorption peaking at 4.85 eV. This corresponds to a transition between an s-like and a p-like states. (B) Shows transitions in the V_O^{+1} center in MgO. The lower energy absorption peaks at 4.70 and comes from excitation of an α spin electron in a gap-state into CB states. The higher energy absorption peaks at 5.26 eV and comes from excitation of electrons in VB states into the unoccupied state in the gap. (C) is the V_O^{+2} defect in MgO. (D), (E), and (F) correspond to the V_O^0, V_O^{+1} and V_O^{+2} centers in m-HfO_2, respectively. All the transitions represented by (E) are from excitations in the alpha channel. Individual transitions (without smearing) are shown by delta functions, in (F) these trnasitions are too small to be seen. The smeared spectra is plotted using Gaussian smearing of $\sigma = 0.2$ eV.

states in the valence band responsible for β transitions. We therefore find that failure to allow the charged defect to fully relax can change absorption energies by as much as 2 eV.

In HfO_2, optical excitations in the α and β spin channels have different energies. To illustrate why, we can look at the electronic structure of the V_O^{+1} defect in HfO_2. The alpha HOMO-LUMO separation is calculated to be 3.6 eV, whereas the beta HOMO-LUMO separation is calculated to be 5.6 eV (very close to the optical band gap value). Thus, when irradiating HfO_2 with photons of sub-bandgap energy, we expect the V_O^{+1} spectrum to be dominated by α spin transitions (transitions from the vacancy state into the CB states, i.e. type 4 in Fig. 1). Indeed we predict that the first optical absorption peak occurs at 2.9 eV and corresponds to the transition of the alpha-spin electron from the gap-state into a quasi-local state in the CB. All the higher energy peaks up to band-gap energy also correspond to excitations of the α-spin electron out of the gap-state and into higher energy CB states. Excitations in the β spin channel are only attainable once we arrive at excitation energies comparable with the band gap.

In both materials the V_O^{+2} defect produces an unoccupied state high in the band gap as well as resonant states in the CB (Fig. 1). In MgO, the optical absorption of the V_O^{+2} center has been predicted[26] to be close to the V_O^0 and V_O^{+1} defects. It is dominated by transitions from the defect-induced states in the valence band into the LUMO defect state located close to the bottom of the CB (type III in Fig. 1) . Therefore, all of the V_O defects in MgO are predicted to have optical absorption peaks near 5 eV. This explains why it is so difficult to distinguish between different charge states of the V_O defect in MgO using optical absorption experiments alone.

In HfO_2, the optical transition energies from the valence band into the V_O^{+2} defect are comparable to the band gap energy and are predominantly of type II in Fig. 1. Optical experiments conducted on HfO_2[24] have detected a 5.2 eV absorption peak which has been attributed to the presence of oxygen vacancies. We predict that the doubly positively charged oxygen vacancy (V_O^{+2}) has an optical absorption peak at 5.3 eV, which is in good agreement with this detected absorption band. We note that the position of the peak predicted in this work is at higher photon energy than 4.94 eV calculated in Ref.[26] using TDDFT in a relatively small embedded cluster. This is consistent with our observation that full account of defect-induced lattice distortion for charged defects is important for predicting correct optical absorption ener-

gies.

C. Photoluminescence energies

As was mentioned above, MgO has a well-established PL band at 2.3 eV attributed to the V_O^0 center[8–10,16]. The life-time of this luminescence is much longer than that for the V_O^+ center, which is caused by a single-electron transition in the doublet state. Therefore the 2.3 eV luminescence of the V_O^0 center could be due to a partially-allowed 2s $\rightarrow$ 1s type and/or triplet-to-singlet transition. The kinetics of this PL is, however, much more complicated than that of the V_O^0 center in CaO, where the lowest relaxed excited state has been shown to have a tetragonal (100) triplet state with fast spin-lattice relaxation (see, for example, Ref.[41]). The PL kinetics in MgO is strongly affected by the presence of H and other impurities and depends on sample preparation[8,16]. Semi-empirical[16] calculations suggest that tetragonal singlet and triplet states are both located very close to the bottom of the CB and that there are two minima in the relaxed excited state corresponding to $^3T_{1u}$ and $^3A_{1g}$ configurations, respectively. The predicted PL energies corresponding to transitions from these two minima are equal to 2.9 eV and 2.2 eV, respectively. The PL peaking at 2.9 eV has been observed experimentally[42] but has an excitation energy at about 7 eV. It has been concluded that the PL peaks at 2.3 eV and 2.9 eV may involve both transitions intrinsic to the V_O^0 center and those caused by electron transfer from impurities[8,16]. We note that the dynamics of similar PL of F centers in alkali halides has been studied in detail[43]. In that case, the transition is allowed due mixing of 2s and 2p terms, with 2s having the lower energy in the relaxed excited state[43].

To shed more light on the nature of excited states, we have calculated the triplet excited states of the V_O^0 center in MgO using the so called ΔSCF method. This computational procedure employs a non-Aufbau occupation of the triplet state in a dielectric to converge the KS equations to an excited state[44**?**] . The total energy and geometry of the triplet excited state of a defect are calculated self-consistently. This approach allows us to predict defect geometries in the electronically excited state (the feature still unavailable in TDDFT in CP2K). The lowest energy triplet state has $^3A_{1g}$ symmetry and the calculated luminescence energy from this state is 2.0 eV. A higher energy triplet state has a geometry formed from a combination of A_{1g} and T_{2g} displacement modes. The calculated PL energy from this state is 2.9 eV. Thus our calculations support the PL model suggested in earlier studies[8,16] with surprising agreement of calculated PL energies.

We used the same approach to investigate the luminescence of the neutral oxygen vacancy in m-HfO_2. In the case of optical excitation of the V_O^0 defect the electron-hole pair remains bound to the vacancy. The predicted triplet-singlet PL energy is 0.8 eV.

The situation is, however, more intriguing in the case of the V_O^{+2} center. It produces an unoccupied state inside the gap close to the bottom of the CB as well as quasi-local states in the VB and CB in both MgO and m-HfO_2. In alkali halides, a singly positively charged anion vacancy (also called an α-center) has a qualitatively similar electronic structure and a characteristic luminescence, which is close in energy to the exciton luminescence (so called α-luminescence) and is attributed to exciton perturbed by the vacancy[45]. The relaxed excited state of this center can be also viewed as an electron transferred into the vacancy and a hole trapped next to the vacancy[46]. Such luminescence has not been observed for V_O^{+2} center in MgO because free excitons in MgO are very mobile and get trapped by impurities. Since excitons and holes have been suggested to self-trap in m-HfO_2[47–49] one could expect creation of α-type luminescence in this material. Recent experiments[27] suggest that 3.6 eV luminescence excited by 5.3 eV photons could be due to charged vacancies in m-HfO_2.

Using the ΔSCF method we investigated the triplet excited state of the V_O^{+2} defect in HfO_2. It is found that the relaxed triplet configuration of the V_O^{+2} center has an electron localized into the vacancy (producing a V_O^{+1} center) and a hole localized in a polaron state elsewhere in the supercell. Holes have been predicted to self-trap in m-HfO_2 at low temperatures[48,50]. Due to repulsion with the positively charged vacancy, the hole cannot sit close to the vacancy - the closest stable separation we find between the hole polaron and the vacancy is approximately 5 Å (see Figure 4). Therefore the localized hole and vacancy can be viewed as two separated defects. In such a system, luminescence due to electron-hole recombination can occur when the electron in the V_+ defect tunnels into the hole polaron via a radiative tunneling transition (RTT). The RTT recombination luminescence of spatially well-separated electron and hole defects has been studied in semiconductors[51] and ionic crystals[52]. It usually occurs between ground electronic states of donor and acceptor.

We predict the photon energy of this emission to be 3.7 eV. Unlike in semiconductors[51], the emission energy does not depend on the defect separation in the range of up to 11 Å (this upper limit originates in the finite size of the supercell) due to dielectric screening in the high-k material. In[53] a range of luminescence peaks between 2.0 and 3.7 eV, attributed to oxygen vacancies have been detected at approximately 7 K using cathodo- and optical luminescence. In another optical experiment[47], conducted at 10 K, weak emission in the range of 2.2 to 3.6 eV has been detected. A recent study[27] also found luminescence peaking near 3.6 eV, again linked to oxygen vacancies. These results are consistent with the optical absorption of the V_O^{+2} defect and the predicted RTT luminescence energy. However, further studies are required to elucidate the nature of experimentally observed peaks.

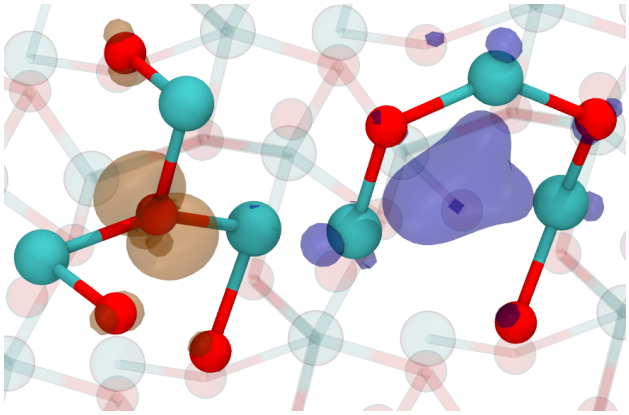

FIG. 4. The relaxed triplet configuration of the V_O^{+2} defect. An electron localises around the vacancy (to create a V_O^{+1} defect) and a hole self-traps elsewhere in the lattice. A range of separations between hole and vacancy are possible. Here, the closest separation configuration is shown. Transparent surfaces show the $|\psi|^2$ of the hole (orange) and electron (blue). The iso-surface value is 0.007. The nearest neighbor atoms of each defect are highlighted.

IV. CONCLUSIONS

To conclude, we used a newly implemented TDDFT algorithm in CP2K to conduct optical absorption calculations on oxygen vacancies in MgO and HfO_2. Using a range of periodic cells We demonstrate that failure to properly describe the geometric structure of a defect significantly affects the predicted absorption energies, potentially by several eV. We confirm the existing models of the nature of optical absorption and photoluminescence of O vacancies in MgO and HfO_2 and predict that the PL at 3.7 eV in HfO_2 excited at 5.2 eV could originate from radiative tunneling transitions between a V_+ center and hole polaron created by this excitation. The results of our calculations are in good agreement with the available experimental data and shed light on the nature of optical absorption and luminescence peaks in these materials. Therefore the use of TDDFT with a hybrid functional, which strikes a good balance between accuracy and computational efficiency, is appropriate for the prediction of the optical properties of defects in other solid state systems.

V. ACKNOWLEDGMENTS

We acknowledge funding provided by the UK Engineering and Physical Sciences Research Council (EPSRC) under grants No. EP/K01739X/1 and EP/P013503/1 and by the Leverhulme Trust RPG-2016-135. J.S. is funded by EPSRC grant no. EP/G036675/1 to the Center for Doctoral Training. Computer facilities on the ARCHER UK National Supercomputing Service have been provided via the UKs HPC Materials Chemistry Consortium (EPSRC Grant No. EP/L000202). Part of this work was funded under the embedded CSE programme of the ARCHER UK National Supercomputing Service (http://www.archer.ac.uk).

VI. APPENDIX

In the linear response (LR) formulation, TDDFT equations can be cast in the form of a non-Hermitian eigenproblem[54]:

$$\begin{pmatrix} A & B \\ B^* & A^* \end{pmatrix} \begin{pmatrix} X_p \\ Y_p \end{pmatrix} = \omega_p \begin{pmatrix} 1 & 0 \\ 0 & -1 \end{pmatrix} \begin{pmatrix} X_p \\ Y_p \end{pmatrix}, \quad (12)$$

where (X_p, Y_p) is an eigenvector and ω_p is a corresponding transition energy. In terms of Kohn-Sham orbitals $\{\phi\}$, the elements of the matrices A and B can be written as[55]:

$$\begin{aligned} A_{ia\sigma,jb\tau} &= A^{\mathrm{E}}_{ia\sigma,jb\tau} + A^{\mathrm{J}}_{ia\sigma,jb\tau} + c_{\mathrm{HFX}} A^{\mathrm{HFX}}_{ia\sigma,jb\tau} + A^{\mathrm{XC}}_{ia\sigma,jb\tau} \\ &= \delta_{ij}\delta_{ab}\delta_{\sigma\tau}(\epsilon_{a\sigma} - \epsilon_{i\sigma}) + (i_\sigma a_\sigma | j_\tau b_\tau) \\ &\quad - c_{\mathrm{HFX}}\delta_{\sigma\tau}(i_\sigma j_\sigma | a_\tau b_\tau) + (i_\sigma a_\sigma | f_{\mathrm{xc};\sigma\tau} | j_\tau b_\tau), \end{aligned} \quad (13)$$

$$\begin{aligned} B_{ia\sigma,jb\tau} &= (i_\sigma a_\sigma | b_\tau j_\tau) - c_{\mathrm{HFX}}\delta_{\sigma\tau}(i_\sigma b_\sigma | a_\tau j_\tau) \\ &\quad + (i_\sigma a_\sigma | f_{\mathrm{xc};\sigma\tau} | b_\tau j_\tau). \end{aligned} \quad (14)$$

Here A^{E}, A^{J}, A^{HFX}, A^{XC} denote orbital energy difference, electron-hole Coulomb, exact-exchange, and exchange-correlation (XC) terms respectively, while notations $(i_\sigma a_\sigma | j_\tau b_\tau)$ and $(i_\sigma a_\sigma | f_{\mathrm{xc};\sigma\tau} | j_\tau b_\tau)$ stand for four-centre electron repulsion integrals (ERIs) and XC-integrals:

$$(i_\sigma a_\sigma | j_\tau b_\tau) = \int \phi^*_{i\sigma}(\mathbf{r})\phi_{a\sigma}(\mathbf{r}) \frac{1}{|\mathbf{r} - \mathbf{r}'|} \phi^*_{j\tau}(\mathbf{r}')\phi_{b\tau}(\mathbf{r}')\mathrm{d}\mathbf{r}\mathrm{d}\mathbf{r}' \quad (15)$$

$$\begin{aligned} (i_\sigma a_\sigma | f_{\mathrm{xc};\sigma\tau} | j_\tau b_\tau) = \int & \phi^*_{i\sigma}(\mathbf{r})\phi_{a\sigma}(\mathbf{r}) f_{\mathrm{xc};\sigma\tau}(\mathbf{r}, \mathbf{r}') \\ & \times \phi^*_{j\tau}(\mathbf{r}')\phi_{b\tau}(\mathbf{r}')\mathrm{d}\mathbf{r}\mathrm{d}\mathbf{r}' \end{aligned} \quad (16)$$

We use the following index convention: i and j label occupied orbitals, a and b stand for virtual orbitals, and σ and τ refer to spin components. Besides, the quantity $\epsilon_{i\sigma}$ stands for the i-th Kohn-Sham orbital energy, and $f_{\mathrm{xc};\sigma\tau}(\mathbf{r}, \mathbf{r}')$ is a response XC-kernel. The explicit expression for the A^{XC} term in Eq. (13) is given in the adiabatic approximation which postulates independence of the XC-functional on time. As such, XC-kernel becomes the second functional derivative of the XC-functional (E_{xc}) over the ground-state electron density ($\rho^{(0)}$)[56]:

$$f_{\mathrm{xc};\sigma\tau}(\mathbf{r}, \mathbf{r}') = \left. \frac{\delta^2 E_{\mathrm{xc}}[\rho](\mathbf{r})}{\delta\rho_\sigma(\mathbf{r}')\delta\rho_\tau(\mathbf{r}')} \right|_{\rho=\rho^{(0)}}. \quad (17)$$

It is important to note that in case of a hybrid exchange functional the exact-exchange term is excluded from the

XC-functional prior taking its functional derivative. For example, in case of a standard PBE0 XC-functional[30] which contains 100% PBE correlation, 75% PBE exchange, and 25% exact-exchange energies, only the first two terms contribute towards the XC-kernel.

As is customary, we also use the Tamm-Dancoff approximation (TDA)[57] which amounts to setting all the elements of the matrix B in Eq. (12) to zero. This simplifies the LR-TDDFT equation by reducing it to a standard Hermitian eigenproblem:

$$AX_p = \omega_p X_p. \tag{18}$$

We use block Davidson method[58] to solve this eigenproblem, as the matrix A itself is a diagonally dominant one and only few excited states are typically in interest.

A significant advantage of the Davidson algorithm follows from its iterative nature. The algorithm approximates target eigenvectors by iteratively refining a set of trial vectors X_p – one vectors for each excited state p in question – and only the action of the response operator on these vectors AX_p needs to be known. In our implementation we use trial vectors in form of contracted response orbitals $\phi^{(1)}_{i;p\sigma}(\mathbf{r})$, which is a linear combination of virtual Kohn-Sham orbitals $\phi_{a;\sigma}(\mathbf{r})$

$$\phi^{(1)}_{i;p\sigma}(\mathbf{r}) = \sum_{a}^{\mathrm{LUMO}} X_{ia;p\sigma}\phi_{a;\sigma}(\mathbf{r}) \tag{19}$$

obtained from solving the ground-state KS-DFT equations. The squared contraction coefficients $|X_{ia;p\sigma}|^2$ thus can be thought as a probability of an electron transition between the i-th occupied and a-th virtual KS orbitals.

By analogy with occupied ground-state KS orbitals $\phi_{i,\sigma}$, the contracted response orbitals are expanded as a linear combination of atomic basis functions $\{\chi\}$:

$$\phi_{i;\sigma}(\mathbf{r}) = \sum_{\mu=1}^{N} C^{(0)}_{\mu i;\sigma}\chi_\mu(\mathbf{r}), \quad \phi^{(1)}_{i;p\sigma}(\mathbf{r}) = \sum_{\mu=1}^{N} C^{(1)}_{\mu i;p\sigma}\chi_\mu(\mathbf{r}), \tag{20}$$

subject to orthogonality conditions:

$$\mathrm{Tr}\left(C^{(0),\mathrm{T}}_{\sigma} S C^{(1)}_{p\sigma}\right) = 0, \tag{21}$$

$$\mathrm{Tr}\left(C^{(1),\mathrm{T}}_{p\uparrow} S C^{(1)}_{q\uparrow}\right) + \mathrm{Tr}\left(C^{(1),\mathrm{T}}_{p\downarrow} S C^{(1)}_{q\downarrow}\right) = \delta_{pq}. \tag{22}$$

where $S_{\mu\nu} = \langle\chi_\mu|\chi_\nu\rangle$ is the overlap matrix, and δ_{pq} is the Kronecker delta. The calculation of the action of the response operator on trial vectors, expressed in the atomic basis set, is then performed in the following steps, which are essentially the same steps as required for building the Kohn-Sham matrix in ground-state DFT using the Gaussian and Plane Wave method[28]:

1. For every spin component σ construct the response density matrix:

$$P^{(1)}_{p\sigma} = \frac{1}{2}\left(C^{(0)}_{\sigma} C^{(1),\mathrm{T}}_{p\sigma} + C^{(1)}_{p\sigma} C^{(0),\mathrm{T}}_{\sigma}\right). \tag{23}$$

The initial guess is formed from energetically ordered single orbital excitations. Note that the response density matrix is not a pure one, as it does not fulfil the idempotent property:

$$P^{(1)}_{p\sigma} S P^{(1)}_{p\sigma} S \neq P^{(1)}_{p\sigma} S.$$

Map the response density onto a real-space grid $P^{(1)}_{p\sigma} \to \rho^{(1)}_{p\sigma}(\mathbf{r})$ and the corresponding reciprocal-space grid by performing the fast Fourier transformation (FFT):

$$\rho^{(1)}_{p\sigma}(\mathbf{G}) = \mathrm{FFT}[\rho^{(1)}_{p\sigma}(\mathbf{r})].$$

2. Compute the energy difference term:

$$A^{\mathrm{E}} C^{(1)}_{p\sigma} = F_\sigma C^{(1)}_{p\sigma} - \epsilon_\sigma S C^{(1)}_{p\sigma}, \tag{24}$$

where F_σ and S are Kohn-Sham and overlap matrices respectively, and ϵ_σ is a diagonal matrix of Kohn-Sham orbital energies.

3. Compute the Coulomb term by

   (a) solving the Poisson equation on the reciprocal grid: $\rho^{(1)}_{p\sigma}(\mathbf{G}) \to v^{(1)}_{p\sigma}(\mathbf{G})$;

   (b) calculating components of the electrostatic potential on the real-space grid using the inverse FFT: $v^{(1)}_{p\sigma}(\mathbf{r}) = \mathrm{FFT}^{-1}[v^{(1)}_{p\sigma}(\mathbf{G})]$.

4. Compute the adiabatic XC term by evaluating the integral:

$$\bar{f}_{\mathrm{xc};p\sigma}(\mathbf{r}) = \sum_{\tau=\uparrow,\downarrow} \eta_\tau \int f_{\mathrm{xc};\sigma\tau}(\mathbf{r},\mathbf{r}')\rho^{(1)}_{p\tau}(\mathbf{r}')\mathrm{d}\mathbf{r}' \tag{25}$$

on the real-space grid. The scaling factors $(\eta_\uparrow, \eta_\downarrow)$ are equal to $(2, 0)$ or $(1, -1)$ for singlet and triplet states computed using spin-unpolarised electron density, or $(1, 1)$ otherwise.

5. Transform the sum of electrostatic potential and the XC term from the grid representation into a matrix representation in the atomic basis set by evaluating expectation values:

$$\left(A^{\mathrm{J}} C^{(1)}_{p\sigma} + A^{\mathrm{XC}} C^{(1)}_{p\sigma}\right)_{\mu\nu} = \int \chi^*_\mu(\mathbf{r})\left(v^{(1)}_{p\sigma}(\mathbf{r}) + \bar{f}_{\mathrm{xc};p\sigma}(\mathbf{r})\right)\chi_\nu(\mathbf{r})\mathrm{d}\mathbf{r}. \tag{26}$$

6. Using precomputed ERIs over atomic basis functions $(\mu\nu|\lambda\xi)$, compute matrix elements of the exact-exchange operator:

$$(K_{p\sigma})_{\mu\lambda} = \sum_{\nu\xi}(\mu\nu|\lambda\xi)\left(P^{(1)}_{p\sigma}\right)_{\nu\xi}. \tag{27}$$

The exact-exchange action term is then calculated as a matrix product scaled by the amount of the exact exchange:

$$c_{\mathrm{HFX}} A^{\mathrm{HFX}} C^{(1)}_{p\sigma} = c_{\mathrm{HFX}} K_{p\sigma} C^{(0)}_{\sigma}. \tag{28}$$

7. When combined with ADMM (see section II B), instead of the previous step compute the matrix elements of the exact-exchange operator in auxiliary basis set $\{\tilde{\chi}\}$ using the auxiliary density matrix $\tilde{P}$ from Eq. (4):

$$\left(\tilde{K}_{p\sigma}\right)_{\tilde{\mu}\tilde{\lambda}} = \sum_{\tilde{\nu}\tilde{\xi}} (\tilde{\mu}\tilde{\nu}|\tilde{\lambda}\tilde{\xi}) \left(\tilde{P}^{(1)}_{p\sigma}\right)_{\tilde{\nu}\tilde{\xi}}, \tag{29}$$

and then project the obtained matrix back to the primary basis set:

$$K_{p\sigma} = O^{\mathrm{T}} \tilde{K}_{p\sigma} O. \tag{30}$$

Repeating steps 4 and 5 we also compute two compensation XC terms using a reference (semi-)local XC-functional in accordance with Eq. (8).

8. All components of the action matrix for the given response wave function (steps 2, 5, and 6) are then summed up. Once obtained for all excited states in question, these action matrices then used in the block Davidson algorithm[58] to compute residuals and to refine the response wave functions.

With no periodic boundary conditions, having the optimised response wave function for the p-th transition Ψ_p one can compute the associated oscillator strength using the classic expression for dipole integrals in the "length" form[54]:

$$f_p = \frac{2}{3}\omega_p \sum_{q=x,y,z} \left|\langle \Psi_p | q | \Psi_0 \rangle\right|^2. \tag{31}$$

The above expression can be recast in terms of contracted expansion coefficients:

$$f_p = \frac{2}{3}\omega_p \sum_{q=x,y,z} \left| \mathrm{Tr}\left[C_p^{(1),\mathrm{T}} S C^{\mathrm{virt.}} C^{\mathrm{virt.},\mathrm{T}} Q_q C^{(0)} \right] \right|^2, \tag{32}$$

where the matrix elements of the dipole operator in atomic basis set are:

$$Q_{q,\mu\nu} = \langle \chi_\mu | q | \chi_\nu \rangle, \tag{33}$$

and $C^{\mathrm{virt.}}$ is a matrix of expansion coefficients of virtual Kohn-Sham orbitals $\phi_{a;\sigma}(\mathbf{r})$ in the atomic basis set. Using the commutation relation between Hamiltonian and position operators

$$[\hat{H}, \hat{\mathbf{r}}] = -\nabla, \tag{34}$$

we can rewrite Eq. (32) in the equivalent "velocity" form:

$$f_p = \frac{2}{3}\omega_p \sum_{q=x,y,z} \left| \mathrm{Tr}\left[C_p^{(1),\mathrm{T}} S C^{\mathrm{virt.}} \left\{ W \otimes (C^{\mathrm{virt.},\mathrm{T}} \frac{\partial S}{\partial q} C^{(0)}) \right\} \right] \right|^2, \tag{35}$$

to make it suitable for periodic boundary conditions. Here W is the inverse energy difference matrix between all virtual (a) and occupied (i) Kohn-Sham orbitals:

$$W_{ai} = (\epsilon_a - \epsilon_i)^{-1}, \tag{36}$$

$\frac{\partial S}{\partial q}$ is a matrix containing the first partial derivative of overlap integrals along the q-th direction:

$$\left(\frac{\partial S}{\partial q}\right)_{\mu\nu} = \langle \chi_\mu | \frac{\partial \chi_\nu}{\partial q} \rangle, \tag{37}$$

and the symbol $\otimes$ denotes the element-wise (Hadamard) product.

[1] A. I. Popov, E. A. Kotomin, and J. Maier, Nuclear Instruments and Methods in Physics Research B **268**, 3084 (2010).
[2] G. Pacchioni, Solid State Sciences **2**, 161 (2000).
[3] A. L. Shluger, A. S. Foster, J. L. Gavartin, and P. V. Sushko, in *Nano and Giga Challenges in Microelectronics*, edited by J. Greer, A. Korkin, and J. Labanowski (Elsevier, 2003) pp. 151–222.
[4] M. V. Ganduglia-Pirovano, A. Hofmann, and J. Sauer, Surface Science Reports **62**, 219 (2007).
[5] Y. Chen, R. T. Williams, and W. A. Sibley, Physical Review **182**, 960 (1969).
[6] R. C. Whited and W. C. Walker, Physical Review Letters **22**, 1428 (1969).
[7] L. A. Kappers, R. L. Kroes, and E. B. Hensley, Physical Review B **1**, 4151 (1970).
[8] G. H. Rosenblatt, M. W. Rowe, G. P. Williams Jr, R. T. Williams, and Y. Chen, Physical Review B **39**, 10309 (1989).
[9] A. Lushchik, T. Kärner, C. Lushchik, E. Vasil'chenko, S. Dolgov, V. Issahanyan, and P. Liblik, Physica Status Solidi (c) **4**, 1084 (2007).
[10] E. Feldbach, R. Jaaniso, M. Kodu, V. P. Denks, A. Kasikov, P. Liblik, A. Maaroos, H. Mändar, and M. Kirm, Journal of Materials Science: Materials in Electronics **20**, 321 (2009).
[11] F. Illas and G. Pacchioni, The Journal of Chemical Physics **108**, 7835 (1998).
[12] C. Sousa and F. Illas, The Journal of Chemical Physics **115**, 1435 (2001).
[13] M. A. Monge, R. Gonzalez, J. E. M. Santiuste, R. Pareja, Y. Chen, E. A. Kotomin, and A. I. Popov, Nuclear Instruments and Methods in Physics Research Section B: Beam Interactions with Materials and Atoms **166**, 220 (2000).
[14] R. González, M. A. Monge, J. E. M. Santiuste, R. Pareja, Y. Chen, E. Kotomin, M. M. Kukla, and A. I. Popov, Physical Review B **59**, 4786 (1999).
[15] P. Rinke, A. Schleife, E. Kioupakis, A. Janotti, C. Rödl, F. Bechstedt, M. Scheffler, and C. G. Van de Walle, Physical Review Letters **108**, 126404 (2012).
[16] G. P. Summers, T. M. Wilson, B. T. Jeffries, H. T. Tohver, Y. Chen, and M. M. Abraham, Physical Review B **27**, 1283 (1983).
[17] T. M. Wilson and R. F. Wood, Journal de Physique Colloques **37**, C7 (1976).
[18] C. H. Lien, Y. S. Chen, H. Y. Lee, P. S. Chen, F. T. Chen, and M.-J. Tsai (IEEE, 2010) pp. 1084–1087.
[19] H. Akinaga and H. Shima, Proceedings of the IEEE **98**, 2237 (2010).
[20] B. Traoré, P. Blaise, E. Vianello, E. Jalaguier, G. Molas, J. F. Nodin, L. Perniola, B. De Salvo, and Y. Nishi, in *Reliability Physics Symposium, 2014 IEEE International* (IEEE, 2014) p. 5E.2.
[21] R. Degraeve, A. Fantini, G. Gorine, P. Roussel, S. Clima, C. Y. Chen, B. Govoreanu, L. Goux, D. Linten, M. Jurczak, *et al.*, in *Reliability Physics Symposium (IRPS), 2016 IEEE International* (IEEE, 2016) p. 6C.1.

[22]R. Öttking, S. Kupke, E. Nadimi, R. Leitsmann, F. Lazarevic, P. Plänitz, G. Roll, S. Slesazeck, M. Trentzsch, and T. Mikolajick, Physica Status Solidi (a) **212**, 547 (2015).
[23]S. R. Bradley, G. Bersuker, and A. L. Shluger, Journal of Physics: Condensed Matter **27**, 415401 (2015).
[24]T. V. Perevalov, V. S. Aliev, V. A. Gritsenko, A. A. Saraev, V. V. Kaichev, E. V. Ivanova, and M. V. Zamoryanskaya, Applied Physics Letters **104**, 071904 (2014).
[25]V. A. Gritsenko, T. V. Perevalov, and D. R. Islamov, Physics Reports **613**, 1 (2016).
[26]D. M. Ramo, J. L. Gavartin, A. L. Shluger, and G. Bersuker, Physical Review B **75**, 205336 (2007).
[27]V. A. Gritsenko, D. R. Islamov, T. V. Perevalov, V. S. Aliev, A. P. Yelisseyev, E. E. Lomonova, V. A. Pustovarov, and A. Chin, The Journal of Physical Chemistry C **120**, 19980 (2016).
[28]J. VandeVondele, M. Krack, F. Mohamed, M. Parrinello, T. Chassaing, and J. Hutter, Computer Physics Communications **167**, 103 (2005).
[29]M. Guidon, J. Hutter, and J. VandeVondele, Journal of Chemical Theory and Computation **5**, 3010 (2009).
[30]C. Adamo and V. Barone, Journal of Chemical Physics **110**, 6158 (1999).
[31]M. Ernzerhof and J. P. Perdew, Journal of Chemical Physics **109**, 3313 (1998).
[32]S. Goedecker, M. Teter, and J. Hutter, Physical Review B **54**, 1703 (1996).
[33]J. VandeVondele and J. Hutter, Journal of Chemical Physics **127**, 114105 (2007).
[34]M. Guidon, J. Hutter, and J. VandeVondele, Journal of Chemical Theory and Computation **6**, 2348 (2010).
[35]P. Merlot, R. Izsák, A. Borgoo, T. Kjærgaard, T. Helgaker, and S. Reine, Journal of Chemical Physics **141**, 094104 (2014).
[36]A. F. Izmaylov and G. E. Scuseria, Journal of Chemical Physics **129**, 034101 (2008).
[37]R. M. Hazen, American Mineralogist **61**, 266 (1976).
[38]R. E. Hann, P. R. Suitch, and J. L. Pentecost, Journal of the American Ceramic Society **68**, C285 (1985).
[39]M. Balog, M. Schieber, M. Michman, and S. Patai, Thin Solid Films **41**, 247 (1977).
[40]L. E. Halliburton, D. L. Cowan, and L. V. Holroyd, Physical Review B **12**, 3408 (1975).
[41]C. J. Krap, M. Glasbeek, and J. D. W. Van Voorst, Physical Review B **17**, 61 (1978).
[42]A. Lushchik, C. Lushchik, K. Schwartz, F. Savikhin, E. Shablonin, A. Shugai, and E. Vasilchenko, Nuclear Instruments and Methods in Physics Research B **277**, 40 (2012).
[43]T. Koyama and T. Suemoto, Reports on Progress in Physics **74**, 076502 (2011).
[44]R. O. Jones and O. Gunnarsson, Reviews of Modern Physics **61**, 689 (1989).
[45]T. Timusk and W. Martienssen, Physical Review **128**, 1656 (1962).
[46]A. L. Shluger and K. Tanimura, Physical Review B **61**, 5392 (2000).
[47]J. Aarik, H. Mändar, M. Kirm, and L. Pung, Thin Solid Films **466**, 41 (2004).
[48]K. P. McKenna, M. J. Wolf, A. L. Shluger, S. Lany, and A. Zunger, Physical Review Letters **108**, 116403 (2012).
[49]D. M. Ramo, P. V. Sushko, and A. L. Shluger, Physical Review B **85**, 024120 (2012).
[50]D. M. Ramo, A. L. Shluger, J. L. Gavartin, and G. Bersuker, Physical Review Letters **99**, 155504 (2007).
[51]A. T. Vink, Journal of Luminescence **9**, 159 (1974).
[52]A. Shluger, E. Kotomin, and L. Kantorovich, Solid State Communications **42**, 749 (1982).
[53]E. V. Ivanova, M. V. Zamoryanskaya, V. A. Pustovarov, V. S. Aliev, V. A. Gritsenko, and A. P. Yelisseyev, Journal of Experimental and Theoretical Physics **120**, 710 (2015).
[54]M. E. Casida, Journal of Molecular Structure: THEOCHEM **914**, 3 (2009).
[55]A. Dreuw, J. L. Weisman, and M. Head-Gordon, Journal of Chemical Physics **119**, 2943 (2003).
[56]M. Iannuzzi, T. Chassaing, T. Wallman, and J. Hutter, CHIMIA International Journal for Chemistry **59**, 499 (2005).
[57]S. Hirata and M. Head-Gordon, Chemical Physics Letters **314**, 291 (1999).
[58]M. Crouzeix, B. Philippe, and M. Sadkane, SIAM Journal on Scientific Computing **15**, 62 (1994).